

Binary neutron-star mergers with Whisky and SACRA: First quantitative comparison of results from independent general-relativistic hydrodynamics codes.

Luca Baiotti,^{1,2} Masaru Shibata,¹ and Tetsuro Yamamoto³

¹ Yukawa Institute for Theoretical Physics, Kyoto University, Kyoto, 606-8502, Japan

² Institute of Laser Engineering, Osaka University, Suita, 565-0871, Japan

³ Yugen Club, Toyama, Shinjuku, Tokyo, 162-0052, Japan

(Dated: September 14, 2010)

We present the first quantitative comparison of two independent general-relativistic hydrodynamics codes, the Whisky code and the SACRA code. We compare the output of simulations starting from the same initial data and carried out with the configuration (numerical methods, grid setup, resolution, gauges) which for each code has been found to give consistent and sufficiently accurate results, in particular in terms of cleanliness of gravitational waveforms. We focus on the quantities that should be conserved during the evolution (rest mass, total mass energy, and total angular momentum) and on the gravitational-wave amplitude and frequency. We find that the results produced by the two codes agree at a reasonable level, with variations in the different quantities but always at better than about 10%.

PACS numbers: 04.25.D-, 04.30.Db, 04.70.Bw, 95.30.Lz, 97.60.Jd

I. INTRODUCTION

Given the absence of astrophysically relevant exact solutions in general relativity and the difficulty to compare results from numerical-relativity codes with empirical observations (or experiments), it is necessary to find alternative ways to assess the capacity of existing codes to faithfully describe the physical phenomena that they are supposed to simulate, and to check the validity of their results. Among the strategies to achieve such a reassuring confirmation, the most widely used are convergence tests and checks of the violations of the physical constraints imposed by the Einstein equations, in particular of the so-called Hamiltonian and momentum constraints, dictated by the choice of the Arnowitt-Deser-Misner (ADM) formalism as a basis for numerical simulations (see Eqs. (10–11) and, *e.g.*, Refs. [1–3]). Another way to increase the probability of having computer codes free from implementation-errors and unaffected by possibly wrong and maybe hidden assumptions is the comparison of the results of codes independently developed by separate individuals or groups.

Since 2005, the year of the breakthrough in numerical relativity [4–6] that made it possible to calculate the late inspiral, merger, and ringdown of a black-hole binary system in full general relativity, and to calculate the gravitational waves produced in the process, various works [7–9] compared the gravitational waveforms computed in vacuum simulations by several codes. Their general conclusion is that the available codes give consistent results (the difference among codes is smaller than the estimated error within each code) and results that are good enough for being of use in the quest for the detection of gravitational waves through presently operating laser interferometers [10–12] or planned detectors [13, 14].

In the present work, with in mind the goals delineated above, we perform and publish for the first time a comparison between the results of two independent finite-difference codes solving the general-relativistic hydrodynamics equations and the Einstein equations: the Whisky code [15–17] and the SACRA code [3]. We include in the comparison also impor-

tant quantities not directly related to the gravitational waveforms, but, while giving a first glimpse of the comparison of the wave properties, we postpone to a future article [18], which may involve a larger number of codes, the detailed analysis of the usefulness of the computed waveforms for current gravitational-wave detectors.

We also restrict our attention to the modeling of a single physical system, the orbital inspiral of two neutron stars (NSs) in irrotational configuration. This system is however one of the most promising candidates for early detection of gravitational radiation and it is seen as the most likely scenario leading to the formation of a black hole surrounded by a massive torus with properties suitable for being the engine powering short-hard gamma-ray bursts [19].

We use a spacelike signature $(-, +, +, +)$ and a system of units in which $c = G = M_{\odot} = 1$ (unless explicitly shown otherwise for convenience). Greek indices are taken to run from 0 to 3, Latin indices from 1 to 3, and we adopt the standard convention for the summation over repeated indices.

II. MATHEMATICAL AND NUMERICAL SETUP

All the details on the mathematical and numerical setup used by the two codes have been discussed in depth in previous works [2, 3, 20]. In what follows, we limit ourselves to a brief overview, while spelling out the differences between the two codes.

The differences in the implementation of the Einstein and hydrodynamics equations between Whisky and SACRA are summarized in Table I.

A. Evolution system for the fields

We evolve the Einstein equations in the Baumgarte-Shapiro-Shibata-Nakamura (BSSN) formalism [21–24].

For the Whisky simulations, all the equations discussed in this section and in the next are solved using the CCATIE

TABLE I: Differences between Whisky and SACRA in the schemes for the evolution of the spacetime and of the hydrodynamics. See text for definitions and further explanations.

	Whisky	SACRA
conformal factor ϕ	evolve ϕ	evolve $\chi \equiv e^{-2\phi}$
primitive matter variables	ρ, v^i, ε	ρ, u_i, ε
evolved matter variables	D, S_i, τ	D, S_i, E
reconstructed matter variables	primitive variables: ρ, v^i, ε	$D, \tilde{u}_i \equiv S_i/D, \varepsilon$
local Riemann solver	Marquina flux formula	central scheme (Kurganov and Tadmor)
atmosphere treatment	constant rest-mass density	exponentially decreasing rest-mass density

code, a three-dimensional finite-differencing code based on the Cactus Computational Toolkit [25]. A detailed presentation of the code and of its convergence properties has been presented in [20]. For tests and details on SACRA, see instead [3].

In the BSSN formalism, the spacetime is first decomposed into three-dimensional spacelike slices, described by a metric γ_{ij} , an extrinsic curvature K_{ij} , and the gauge functions α (lapse) and β^i (shift) (see Sec. II B for details on how we treat gauges and [26] for a general description of the 3 + 1 split). The standard 3+1 formulation is then modified by introducing different variables as follows. The three-metric γ_{ij} is conformally transformed via

$$\phi = \frac{1}{12} \ln \det \gamma_{ij}, \quad \tilde{\gamma}_{ij} = e^{-4\phi} \gamma_{ij}, \quad (1)$$

and the conformal factor ϕ (in Whisky/CCATIE) or a function of it ($\chi \equiv e^{-2\phi}$, in SACRA) is evolved as an independent variable, while $\tilde{\gamma}_{ij}$ is subject to the constraint $\det \tilde{\gamma}_{ij} = 1$. The extrinsic curvature is subjected to the same conformal transformation and its trace K is evolved as an independent variable. That is, in place of K_{ij} we evolve:

$$K \equiv \text{tr } K_{ij} = \gamma^{ij} K_{ij}, \quad \tilde{A}_{ij} = e^{-4\phi} (K_{ij} - \frac{1}{3} \gamma_{ij} K), \quad (2)$$

with $\text{tr } \tilde{A}_{ij} = 0$. Finally, new evolution variables

$$\tilde{\Gamma}^i = \tilde{\gamma}^{jk} \tilde{\Gamma}_{jk}^i = -\tilde{\gamma}_{,j}^{ij} \quad (3)$$

are introduced, defined in terms of the Christoffel symbols of the conformal three-metric.

The Einstein equations specify a well-known set of evolu-

tion equations for the listed variables. They are:

$$(\partial_t - \mathcal{L}_\beta) \tilde{\gamma}_{ij} = -2\alpha \tilde{A}_{ij}, \quad (4)$$

$$(\partial_t - \mathcal{L}_\beta) \phi = -\frac{1}{6} \alpha K, \text{ or } (\partial_t - \mathcal{L}_\beta) \chi = \frac{1}{3} \alpha \chi K, \quad (5)$$

$$(\partial_t - \mathcal{L}_\beta) \tilde{A}_{ij} = e^{-4\phi} [-\mathcal{D}_i \mathcal{D}_j \alpha + \alpha (R_{ij} - 8\pi \mathcal{S}_{ij})]^{TF} + \alpha (K \tilde{A}_{ij} - 2\tilde{A}_{ik} \tilde{A}_{,j}^k), \quad (6)$$

$$(\partial_t - \mathcal{L}_\beta) K = -\mathcal{D}^i \mathcal{D}_i \alpha + \alpha [\tilde{A}_{ij} \tilde{A}^{ij} + \frac{1}{3} K^2 + 4\pi (\rho_{ADM} + \mathcal{S})], \quad (7)$$

$$\begin{aligned} \partial_t \tilde{\Gamma}^i &= \tilde{\gamma}^{jk} \partial_j \partial_k \beta^i + \frac{1}{3} \tilde{\gamma}^{ij} \partial_j \partial_k \beta^k + \beta^j \partial_j \tilde{\Gamma}^i - \tilde{\Gamma}^j \partial_j \beta^i \\ &\quad + \frac{2}{3} \tilde{\Gamma}^i \partial_j \beta^j - 2\tilde{A}^{ij} \partial_j \alpha + 2\alpha (\tilde{\Gamma}^i_{jk} \tilde{A}^{jk} + 6\tilde{A}^{ij} \partial_j \phi \\ &\quad - \frac{2}{3} \tilde{\gamma}^{ij} \partial_j K - 8\pi \tilde{\gamma}^{ij} \mathcal{S}_j), \end{aligned} \quad (8)$$

where R_{ij} is the three-dimensional Ricci tensor, \mathcal{D}_i the covariant derivative associated with the three metric γ_{ij} , “TF” indicates the trace-free part of tensor objects, $\mathcal{S} \equiv \gamma^{ij} \mathcal{S}_{ij}$, and ρ_{ADM} , \mathcal{S}_j , and \mathcal{S}_{ij} are the matter source terms defined as

$$\begin{aligned} \rho_{ADM} &\equiv n_\alpha n_\beta T^{\alpha\beta}, \\ \mathcal{S}_i &\equiv -\gamma_{i\alpha} n_\beta T^{\alpha\beta}, \\ \mathcal{S}_{ij} &\equiv \gamma_{i\alpha} \gamma_{j\beta} T^{\alpha\beta}, \end{aligned} \quad (9)$$

where $n_\alpha \equiv (-\alpha, 0, 0, 0)$ is the future-pointing four-vector orthonormal to the spacelike hypersurface and $T^{\alpha\beta}$ is the stress-energy tensor for a perfect fluid (cf. Eqs. [27]). The Einstein equations also lead to a set of physical constraint equations that are satisfied within each spacelike slice,

$$\mathcal{H} \equiv R^{(3)} + K^2 - K_{ij} K^{ij} - 16\pi \rho_{ADM} = 0, \quad (10)$$

$$\mathcal{M}^i \equiv \mathcal{D}_j (K^{ij} - \gamma^{ij} K) - 8\pi \mathcal{S}^i = 0, \quad (11)$$

which are usually referred to as Hamiltonian and momentum constraints, respectively. Here $R^{(3)} = R_{ij} \gamma^{ij}$ is the Ricci scalar on a three-dimensional timeslice. Our specific choice

of evolution variables introduces five additional constraints,

$$\det \tilde{\gamma}_{ij} = 1, \quad (12)$$

$$\text{tr } \tilde{A}_{ij} = 0, \quad (13)$$

$$\tilde{\Gamma}^i = \tilde{\gamma}^{jk} \tilde{\Gamma}_{jk}^i. \quad (14)$$

Our codes actively enforce the algebraic constraints (12) and (13). Specifically, after every time evolution, we perform a reset as follows:

$$\tilde{\gamma}_{ij} \rightarrow [\det(\tilde{\gamma}_{ij})]^{-1/3} \tilde{\gamma}_{ij}, \quad (15)$$

$$\tilde{A}_{ij} \rightarrow [\det(\tilde{\gamma}_{ij})]^{-1/3} \tilde{A}_{ij} - \frac{1}{3} \tilde{\gamma}_{ij} \text{Tr}(\tilde{A}_{ij}), \quad (16)$$

$$K \rightarrow K + \text{Tr}(\tilde{A}_{ij}). \quad (17)$$

In SACRA, the additional resetting

$$e^{-2\phi} \rightarrow [\det(\tilde{\gamma}_{ij})]^{-1/6} e^{-2\phi} \quad (18)$$

is performed. We note that in these adjustments γ_{ij} and K_{ij} are unchanged.

The remaining constraints, \mathcal{H} , \mathcal{M}^i , and (14), are not actively enforced and can be used as monitors of the accuracy of our numerical solution. See [27] for a more comprehensive discussion of these points.

B. Gauges

We specify the gauge in terms of the standard ADM lapse function, α , and shift vector, β^i [28]. We evolve the lapse according to the “1 + log” slicing condition [29]:

$$\partial_t \alpha - \beta^i \partial_i \alpha = -2\alpha K. \quad (19)$$

The shift is evolved using the hyperbolic $\tilde{\Gamma}$ -driver condition [27]

$$\partial_t \beta^i - \beta^j \partial_j \beta^i = \frac{3}{4} B^i, \quad (20)$$

$$\partial_t B^i - \beta^j \partial_j B^i = \partial_t \tilde{\Gamma}^i - \beta^j \partial_j \tilde{\Gamma}^i - \eta B^i, \quad (21)$$

where η is a parameter which acts as a damping coefficient. We set it to be constant and $\approx 3/M_b$, where M_b is the baryon mass of one of the stars (for the simulations made with Whisky in the present work, the results do not change appreciably if η is changed at least within a factor 2 of the above value). The advection terms on the right-hand sides of these equations have been suggested in [30–32].

C. Apparent horizons and gravitational waves

After the merger, the apparent horizon (AH) formed during the simulation is located every few timesteps during the evolution. In Whisky this computation is performed both with the AHFinderDirect code of [33, 34] and in the isolated and dynamical-horizon frameworks [35–39]. In

SACRA the AH is located as reported in [3].

For the results reported in the present work, both codes extract the gravitational waves using the Newman-Penrose formalism, which provides a convenient representation for a number of radiation-related quantities as spin-weighted scalars. In particular, the curvature scalar

$$\Psi_4 \equiv -C_{\alpha\beta\gamma\delta} n^\alpha \bar{m}^\beta n^\gamma \bar{m}^\delta \quad (22)$$

is defined as a particular component of the Weyl curvature tensor $C_{\alpha\beta\gamma\delta}$ projected onto a given null frame $\{\mathbf{l}, \mathbf{n}, \mathbf{m}, \bar{\mathbf{m}}\}$ and can be identified with the gravitational radiation if a suitable frame is chosen at the extraction radius. In practice, we define an orthonormal basis in the three-space $(\hat{r}, \hat{\theta}, \hat{\phi})$, centered on the Cartesian origin and oriented with poles along \hat{z} . The normal to the slice defines a timelike vector \hat{t} , from which we construct the null frame

$$\mathbf{l} = \frac{1}{\sqrt{2}}(\hat{t} - \hat{r}), \quad \mathbf{n} = \frac{1}{\sqrt{2}}(\hat{t} + \hat{r}), \quad \mathbf{m} = \frac{1}{\sqrt{2}}(\hat{\theta} - i\hat{\phi}). \quad (23)$$

We then calculate Ψ_4 via a reformulation of (22) in terms of ADM variables on the slice [40]:

$$\Psi_4 = C_{ij} \bar{m}^i \bar{m}^j, \quad (24)$$

where

$$C_{ij} \equiv R_{ij} - KK_{ij} + K_i^k K_{kj} - i\epsilon_{ijk} \nabla_l K_{jk} \quad (25)$$

and ϵ_{ijk} is the Levi-Civita symbol. The gravitational-wave polarization amplitudes h_+ and h_\times are then related to Ψ_4 by time integrals [41]:

$$\ddot{h}_+ - i\ddot{h}_\times = \Psi_4, \quad (26)$$

where the double overdot stands for the second-order time derivative. Caution should be taken when performing such integrals [42].

For the extraction of the gravitational-wave signal, both codes also implement an independent method, which is based on the measurements of the nonspherical gauge-invariant metric perturbations of a background spacetime [43]. The wave data obtained in this way give results compatible with the ones obtained with the Newman-Penrose formalism and are not reported here.

D. Evolution system for the matter

Both codes adopt a *flux-conservative* formulation of the hydrodynamics equations [44–46], in which the set of conservation equations for the stress-energy tensor $T^{\mu\nu} = \rho u^\mu u^\nu + pg^{\mu\nu}$ and for the matter current density $J^\mu = \rho u^\mu$ (see below for definitions), namely

$$\nabla_\mu T^{\mu\nu} = 0, \quad \nabla_\mu J^\mu = 0, \quad (27)$$

is written in a hyperbolic, first-order, flux-conservative form of the type

$$\partial_t \mathbf{q} + \partial_i \mathbf{f}^{(i)}(\mathbf{q}) = \mathbf{s}(\mathbf{q}), \quad (28)$$

where $\mathbf{f}^{(i)}(\mathbf{q})$ and $\mathbf{s}(\mathbf{q})$ are the flux vectors and source terms, respectively [47]. Note that the right-hand side (the source terms) does not depend on derivatives of the stress-energy tensor. Furthermore, while the system (28) is not strictly hyperbolic, strong hyperbolicity is recovered in a flat spacetime, where $\mathbf{s}(\mathbf{q}) = 0$.

The primitive hydrodynamical variables are the rest-mass density ρ , the specific internal energy ε measured in the rest-frame of the fluid, and the fluid three-velocity (defined as $v^i = u^i/W + \beta^i/\alpha$ (contravariant components) in Whisky and as u_i (covariant components) in SACRA, where u^μ is the four-velocity measured by a local zero-angular-momentum observer; SACRA defines contravariant components of the three-velocity as $V^i = u^i/u^0$). The Lorentz factor is defined as

$$\begin{aligned} W &\equiv \alpha u^0 = (1 + \gamma^{ij} u_i u_j)^{1/2} \\ &= (1 - \gamma_{ij} v^i v^j)^{-1/2}. \end{aligned} \quad (29)$$

There is then an equation of state (EoS) relating pressure, rest-mass density and internal-energy density.

Following [45], in order to write system (27) in the form of system (28), the primitive variables are mapped to a set of *conserved* variables $\mathbf{q} \equiv (D, S_i, E)$ via the relations

$$\begin{aligned} D &\equiv \sqrt{\gamma} W \rho = e^{6\phi} W \rho, \\ S_i &\equiv D \tilde{u}_i = \sqrt{\gamma} \rho h W^2 v_i \\ E &\equiv \sqrt{\gamma} (\rho h W^2 - p) \equiv \tau + D \equiv D \tilde{e}, \end{aligned} \quad (30)$$

where $h \equiv 1 + \varepsilon + p/\rho$ is the specific enthalpy, $\tilde{u}_i \equiv h u_i$ is the specific momentum, and $\tilde{e} \equiv h W - p/(\rho W)$ is the specific energy.

In this approach, all variables \mathbf{q} are represented on the numerical grid by cell-integral averages. The functions that the variables \mathbf{q} represent are then *reconstructed* within each cell, usually by piecewise polynomials, in a way that preserves conservation of the variables \mathbf{q} [48]. This operation produces two values at each cell boundary, which are then used as initial data for the local Riemann problems, whose (approximate) solution gives the fluxes through the cell boundaries. A method-of-lines approach [48], which reduces the partial differential equations (28) to a set of ordinary differential equations that can be evolved using standard numerical methods, such as Runge-Kutta or the iterative Crank-Nicholson schemes [49, 50], is used to update the equations in time (see [15] for further details). Here, we employ the 4th-order Runge-Kutta method (see below).

Various reconstruction methods are implemented in Whisky and SACRA, but here we always use the piecewise parabolic method (PPM) [51]. Both codes implement the scheme of Kurganov-Tadmor [52] (which is a variation of the HLLE approximate Riemann solver [53]), but Whisky gets better results employing the Marquina flux formula [54] (see [15, 16] for a more detailed discussion). A comparison among different numerical methods in binary-evolution simulations was reported in [2, 55].

There are differences between Whisky and SACRA in several implementation choices. In Whisky, the variables whose

evolution is computed are D , S_i , and $\tau \equiv E - D$. SACRA adopts as evolution variables D , S_i , and E . Furthermore, the PPM reconstruction is performed by SACRA on the variables ρ , $\tilde{u}_i = S_i/D$, and ε , while Whisky reconstructs the primitive variables ρ , v^i , and ε .

Other differences are present in the conversion from the evolved conservative variables back to the primitive variables, which are used to calculate the fluxes and the source terms of the equations. Such a conversion cannot be given in an analytical closed form (except in certain special circumstances).

Whisky implements the following procedure to do the conversion. One writes an equation for the pressure

$$p - \bar{p}[\rho(\mathbf{q}, p), \varepsilon(\mathbf{q}, p)] = 0, \quad (31)$$

where p is the value of the pressure to be found and $\bar{p}[\rho(\mathbf{q}, p), \varepsilon(\mathbf{q}, p)]$ is the pressure as obtained through the EoS in terms of the updated conserved variables \mathbf{q} and of p itself. This is done by inverting (30) to express ρ and ε in terms of the conserved variables and of the pressure only:

$$\rho = \frac{D}{\tau + p + D} \sqrt{(\tau + p + D)^2 - S^2}, \quad (32)$$

$$\varepsilon = D^{-1} \left[\sqrt{(\tau + p + D)^2 - S^2} - p \bar{W} - D \right], \quad (33)$$

where

$$\bar{W} = \frac{\tau + p + D}{\sqrt{(\tau + p + D)^2 - S^2}} \quad (34)$$

is the Lorentz factor, expressed in terms of the conserved variables, and

$$S^2 \equiv \gamma^{ij} S_i S_j. \quad (35)$$

Then (31) is solved numerically. In Whisky we use a Newton-Raphson root finder, for which we need the derivative of the function with respect to the dependent variable, *i.e.* the pressure. This is given by

$$\begin{aligned} \frac{d}{dp} \left\{ p - \bar{p}[\rho(\mathbf{q}, p), \varepsilon(\mathbf{q}, p)] \right\} \\ = 1 - \frac{\partial \bar{p}(\rho, \varepsilon)}{\partial \rho} \frac{\partial \rho}{\partial p} - \frac{\partial \bar{p}(\rho, \varepsilon)}{\partial \varepsilon} \frac{\partial \varepsilon}{\partial p}, \end{aligned} \quad (36)$$

where

$$\frac{\partial \rho}{\partial p} = \frac{DS^2}{\sqrt{(\tau + p + D)^2 - S^2}(\tau + p + D)^2}, \quad (37)$$

$$\frac{\partial \varepsilon}{\partial p} = \frac{pS^2}{\rho [(\tau + p + D)^2 - S^2](\tau + p + D)}, \quad (38)$$

and where $\partial \bar{p}/\partial \rho$ and $\partial \bar{p}/\partial \varepsilon$ are given by the EoS. Once the pressure is found, the other variables follow simply.

In SACRA, the conversion is performed in the following way. From the normalization relation $u^\mu u_\mu = -1$, W is expressed in terms of h and of the evolved values of $\tilde{u}_i (= S_i/D)$ and γ^{ij} :

$$W^2 = 1 + \frac{\gamma^{ij} \tilde{u}_i \tilde{u}_j}{h^2}. \quad (39)$$

For the EoSs chosen in the present work, h is regarded as a function of W for the evolved values of D , \tilde{e} , and ϕ because of the relation $\tilde{e} = hW - pe^{6\phi}/D$ and of the fact that p is written as a function of h , $\rho (= De^{-6\phi}/W)$, and W as $p = p(h, \rho) = p(h, W)$. Substituting the resulting relation for $h = h(W)$ into Eq. (39), we obtain a one-dimensional algebraic equation for W both for the Γ -law EoS and the piecewise-polytropic EoS (see Sec. II D 2). We solve this derived equation using the Newton-Raphson method, for which we need to take a derivative of the equation $F(W) = 0$ with respect to W . This is rather straightforward, and straightforward is also the determination of the variables h , ε , and P , once the equation for W is solved.

1. Treatment of the atmosphere

At least mathematically, the region outside our initial stellar models is assumed to be perfect vacuum. Independently of whether this represents a physically realistic description of a compact star, the vacuum represents a singular limit of any conservative scheme for hydrodynamical evolution and must be treated artificially. Both codes follow a standard approach in computational fluid-dynamics, that is the addition of a tenuous “atmosphere” filling the computational domain outside the star.

Of course, the density of the atmosphere should be as small as possible, in order to avoid spurious effects. The evolution of the hydrodynamical equations in grid zones where the atmosphere is present is the same as the one used in the bulk of the flow. When the rest-mass density in a grid zone falls below the threshold set for the atmosphere, that grid zone is not updated in time and the values of its rest-mass density, internal-energy density, and velocity are set to those of the atmosphere.

Both codes treat the atmosphere as a zero-coordinate-velocity perfect fluid governed by a polytropic EoS with the same adiabatic index used for the bulk matter, or, in case of the piecewise-polytropic EoS (see Sec. II D 2), the same adiabatic index as the one used in the outer parts of the star¹. However, the values of the rest-mass density assigned to the atmosphere are different. In Whisky, the rest-mass density is set to be constant and several (10 in the present simulations) orders of magnitude smaller than the initial maximum rest-mass density ρ_{\max} [2, 15, 16].

In SACRA the rest-mass density is assigned as

$$\rho = \begin{cases} \rho_{\text{atmo}} & r \leq r_0, \\ \rho_{\text{atmo}} e^{1-r/r_0} & r > r_0, \end{cases} \quad (40)$$

where $\rho_{\text{atmo}} = \rho_{\max} \times 10^{-9}$ is chosen. r_0 is a coordinate radius of about $10-20M_{\text{ADM}}$, where M_{ADM} is the ADM mass of the system. In both codes, also the internal-energy density ε is then recomputed from ρ according to the polytropic EoS.

For both codes, with such a choice of parameters, the rest mass of the atmosphere is at least a factor 10^{-5} smaller than the rest mass of the NSs. Thus, spurious effects due to the presence of the atmosphere, such as accretion of the atmosphere onto the NSs and the black hole, the resulting dragging effect against orbital motion, gravitational effects, and effects on the formation and dynamics of the disk around the merged object play a negligible role in the present context.

2. Equations of state

In this work we present results obtained with two EoSs: a simple “ Γ -law” or “ideal-fluid” EoS and a piecewise-polytropic EoS [56]. For the ideal-fluid EoS, the pressure is given as

$$p = (\Gamma - 1)\rho\varepsilon, \quad (41)$$

where Γ is the adiabatic index. When using the ideal-fluid EoS (41), nonisentropic changes can take place in the fluid and, in particular, shocks (which are always present in the mergers and which may play important roles) are allowed to transfer kinetic energy to internal energy. On the other hand, a carefully chosen piecewise-polytropic EoS may mimic more closely a realistic EoS. The parametrised EoS we consider consists of two polytropes interfacing at a density ρ_0 . The relations between the hydrodynamical quantities are ($i = 0, 1$) [56]

$$p = K_i \rho^{\Gamma_i}, \quad (42)$$

$$\varepsilon = (1 + a_i)\rho + \frac{K_i}{\Gamma_i - 1}\rho^{\Gamma_i}, \quad (43)$$

where K_i are the polytropic coefficients, and Γ_i are the polytropic exponents in the different intervals of rest-mass density. Furthermore, the constants a_i , which guarantee continuity, are

$$a_0 = 0, \quad (44)$$

$$a_1 = \frac{\varepsilon(\rho_0)}{\rho_0} - 1 - \frac{K_1}{\Gamma_1 - 1}\rho_0^{\Gamma_1 - 1}. \quad (45)$$

In our simulations we used the parameters of model B of [57], namely:

$$\rho_0 = 1.630497500125504 \times 10^{14} \text{ g cm}^{-3}, \quad (46)$$

$$\begin{aligned} 0 < \rho < \rho_0 : \quad & \Gamma_0 = 1.35692395, \\ & K_0 = 0.35938266 \times 10^{14} \text{ cgs units}, \\ \rho > \rho_0 : \quad & \Gamma_1 = 3.0, \\ & K_1 = 0.15982116 \times 10^{-9} \text{ cgs units}, \\ & a_1 = 0.01088158737430845. \end{aligned}$$

In the presence of shock heating, part of the kinetic energy is converted into thermal energy. To model this property, the original piecewise-polytropic EoS is modified by adding a thermal contribution to the pressure

$$P_{\text{th}} = (\Gamma_{\text{th}} - 1)\rho(\varepsilon - \varepsilon_0), \quad (47)$$

¹ In this case, also the polytropic constant K for the atmosphere is chosen to be the same as the one in the outer parts of the star.

TABLE II: Differences in the implementation of the AMR of SACRA and Whisky. See text for definitions and further explanations.

	Whisky	SACRA
prolonged and restricted variables	conserved variables: D, S_i, τ	$D, \tilde{u}_i (= S_i/D), h$
interpolation for the prolongation of the hydrodynamical variables	ENO: 3 rd order in space, 2 nd order in time	Lagrangian: 5 th order in space (reduced to 1 st order in case of failure), 2 nd order in time (reduced to 1 st order at extrema)
buffer zones	12	6
overlapping same-level grids are	evolved as a single grid	evolved independently (but using the average of the values of the two grids at overlapping points)

where Γ_{th} is the adiabatic index for this correction and ε_0 is given by Eq. (43). In the absence of shocks, ε is equal to ε_0 and thus $P_{\text{th}} = 0$. In the simulations of this work SACRA has adopted $\Gamma_{\text{th}} = \Gamma_0$ while in Whisky the thermal correction was not applied ($P_{\text{th}} = 0$). As the figures of this work show, at least in the inspiral phase the difference in the adopted EoS does not have an influence.

E. Adaptive Mesh Refinement

There are similarities and differences in the implementation of the adaptive mesh refinement (AMR) in the two codes. In the following we spell them out in detail.

Both codes employ a vertex-centered Berger–Oliger [58] mesh-refinement scheme adopting nested grids with a 2 : 1 refinement factor for successive grid levels. In the simulations made for the present work both codes used a set of coarser fixed grids and finer moving grids, centered around each star. Whisky makes use of the Carpet mesh-refinement driver [59]. The higher-resolution moving grids are centered around the local maximum in the rest-mass density ρ of each star. In SACRA, instead, the grids are centered around the local maximum of the conserved variable D .

Both codes employ centered 4th-order finite-differencing in space for evaluating spatial derivatives of the geometric quantities, except for the shift advection terms that are calculated with upwinding derivatives to improve accuracy. For the time integration, the 4th-order Runge–Kutta scheme is adopted. To evolve quantities near the refinement boundaries of a refined grid, both codes introduce buffer zones, where the variables are computed (“prolonged” and “restricted”) in a special way and not with the time-update scheme used for all other non-refinement-boundary points.

In Whisky/Carpet, we use 12 buffer points, 3 for each substep of the adopted time-integration scheme. The values of the needed quantities at the buffer points are computed from the coarser grid through interpolation as follows: For the spacetime variables, 5th-order Lagrangian interpolation in space and 2nd-order Lagrangian interpolation in time are used; For the hydrodynamical variables, 3rd-order ENO [60] interpolation in space and 2nd-order ENO interpolation in time are used. The prolonged and restricted variables are the conserved evolved ones: D, S_i , and τ . The interpolation is done whenever the first Runge–Kutta time integration is being carried out.

In SACRA both prolongation and restriction are carried out on $D, \tilde{u}_i (= S_i/D)$, and h . Following [61], 6 buffer points are introduced. The quantities at the buffer zones are provided from the corresponding coarser domain by the following procedure. For space interpolation, 5th-order centered Lagrangian interpolation in space is carried out using the nearby 6 points of the coarser grid. This is done both for spacetime and hydrodynamics variables. For the latter, this interpolation scheme could fail, in particular in the vicinity of the surface of the stars, where D is small and varies steeply. The reason for this possible failure is that the interpolation may give a negative, and so unphysical, value of D or $h - 1$. If the 5th-order Lagrange interpolation produces $D < D_{\min}$ or $h < 1$, 1st-order (i.e., linear) interpolation is adopted. D_{\min} is chosen to be $D_{\max}/10^9$, where D_{\max} is the initial maximum value of D . Linear interpolation cannot be used in general for all points because it is too dissipative. As in Whisky the interpolation is also done whenever the first Runge–Kutta time integration is being carried out.

For the update of the buffer zones SACRA implements, instead, the following: i) For the inner three buffer points all the quantities are evolved using the 4th-order finite-differencing scheme. Since there is a sufficient number of buffer points to solve the evolution equations in the inner three buffer points, no interpolation is necessary; ii) For the fourth buffer point, all the quantities are evolved using a 4th-order finite-differencing scheme with no interpolation, except for the transport terms for the geometry such as $\beta^k \partial_k \tilde{\gamma}_{ij}$, for which 2nd-order finite differencing is employed when β^k has an unfavorable sign; iii) For the two outer buffer points, 2nd-order Lagrangian interpolation in time of the coarser-grid quantities is carried out. This time-integration procedure is applied to both spacetime and hydrodynamical variables, but for the latter there is an additional check.

The interpolated value at a finer-grid time step is obtained from the values at the three time levels of the coarser grid, say, $n - 1$, n , and $n + 1$ (note that n does not denote the Runge–Kutta time step). The interpolation is necessary for determining the values at a time t that satisfies $t^n < t < t^{n+1}$. Defining Q as D, \tilde{u}_i , or h , and Q^n as the value of the variable Q at time t^n , SACRA checks whether $(Q^{n+1} - Q^n)(Q^n - Q^{n-1}) < 0$ and if so adopts 1st-order interpolation, using only Q^{n+1} and Q^n . Namely, a limiter procedure is introduced. This robust prescription provides numerical stability [3].

The two domains in the finer levels often overlap. In such cases, the values of all quantities should agree with each other,

TABLE III: Properties of the initial data: proper separation between the centers of the stars d/M_{ADM} ; baryon mass M_b of each star in units of solar mass; total ADM mass M_{ADM} in units of solar mass, as measured on the finite-difference grid; total ADM mass \tilde{M}_{ADM} in units of solar mass, as provided by the Meudon initial data; angular momentum J , as measured on the finite-difference grid; angular momentum \tilde{J} , as provided by the Meudon initial data; initial orbital angular velocity Ω_0 ; mean coordinate equatorial radius of each star r_e along the line connecting the two stars; maximum rest-mass density of a star ρ_{max} . The columns for M_{ADM} and J contain the value for Whisky (left) and the one for SACRA (right). Note that the values of M_{ADM} and J are computed through a volume integral in Whisky, while in SACRA they are computed through the extrapolation to $r \rightarrow \infty$ of the ADM masses and angular momenta calculated as surface integrals at finite radii r .

EoS for the model	d/M_{ADM}	M_b (M_\odot)	M_{ADM} (M_\odot)	\tilde{M}_{ADM} (M_\odot)	J ($\times 10^{49} \text{ g cm}^2/\text{s}$)	\tilde{J} ($\times 10^{49} \text{ g cm}^2/\text{s}$)	Ω_0 (rad/ms)	r_e (km)	ρ_{max} (g/cm^3)
Ideal fluid ($\Gamma = 2$)	12.6	1.779	3.251, 3.256	3.233	8.921, 8.930	8.922	1.906	12.23	7.58×10^{14}
Piecewise polytropic	15.4	1.502	2.676, 2.680	2.668	6.492, 6.506	6.491	1.664	8.48	9.77×10^{14}

but, since in SACRA the evolution equations for the two domains are solved independently, the values do not always agree exactly. Let us denote with Q_1 and Q_2 the values on the two domains of an individual refinement level. In order to guarantee that they are the same, in SACRA the average of the two values is used: $Q_1 = Q_2 \rightarrow (Q_1 + Q_2)/2$. When a buffer point of one of the two domains overlaps with a point in the main region of the other domain, the values at the point of the main region are copied to those at the buffer point. When two buffer zones overlap at some points, the simple averaging described above is again used.

In Whisky, when domains of the same refinement level would overlap, the whole level is automatically resplit in (smaller and more numerous) nonoverlapping domains, so in practice they continue to be evolved as a single grid, without requiring averaging. For more details on the Carpet code see [59].

For both codes, at the outer boundaries of the coarsest refinement level, an outgoing boundary condition is imposed for all the geometric variables. The outgoing boundary condition is the same as that suggested by Shibata and Nakamura [22]. Flat boundary conditions are applied to the matter variables.

Both codes can add artificial dissipation to the source terms of the Einstein equations. In particular, for the schemes presented in this work, they could use 5th-order Kreiss-Oliger-type dissipation [62] as $Q_l \rightarrow Q_l - \sigma h_l^6 Q_l^{(6)}$ where Q_l is a quantity in the l -th level, h_l is the spacing of the l -th level, $Q_l^{(6)}$ is the sum of the sixth derivatives along the x , y , and z axis directions, and σ is a constant of order 0.1. The results of the present work were obtained without artificial dissipation for SACRA and with artificial dissipation for Whisky.

Standard SACRA simulations for NS-NS binaries are performed with 7 or 8 refinement levels, in particular 3 or 4 coarser levels composed of one domain and 4 finer levels composed of two domains. The time step for each refinement level, dt_l , is determined as follows:

$$dt_l = \begin{cases} h_2/2 & \text{for } 0 \leq l \leq 2 \\ h_l/2 & \text{for } 2 < l \leq L-1. \end{cases} \quad (48)$$

Namely, the Courant number (expressed in terms of the speed of light) is 1/2 for the finer refinement levels with $l \geq 2$, whereas for the coarser levels, it is smaller than 1/2. The reason why a smaller Courant number is chosen for the coarser levels is that with a Courant number as high as 1/2, numerical

instabilities occur near the outer boundary. This is an inherent problem of the adopted $\tilde{\Gamma}$ -driver gauge condition [?] and it does not appear in the Whisky simulations of the present work only because the resolution in the coarsest grids is still high enough.

In standard Whisky simulations for binary systems 6 refinement levels are used, the two finest of which move following the stars. In addition to the moving grids, a set of refined but fixed grids is set up at the center of the computational domain so as to capture the details of the Kelvin-Helmholtz instability (see [2]). The Courant factor is 0.35 for all levels.

In the Whisky simulations for the present work, a reflection symmetry condition across the $z = 0$ plane and a π -symmetry condition² across the $x = 0$ plane are used, while SACRA adopts only the reflection symmetry across the z plane.

The differences in the implementation of AMR between SACRA and Whisky are summarized in Table II.

F. Initial data

The initial configurations for our relativistic-star binary simulations are produced using the multidomain spectral-method code, LORENE, which was originally written by the group working at the Observatoire de Paris-Meudon [63, 64] and which is publicly available [65]. Specific routines are used to transform the solution from spherical coordinates to a Cartesian grid of the desired dimensions and shape.

These initial data, which we refer to also as the “Meudon data”, are obtained under the assumptions of quasiequilibrium and of conformally-flat spatial metric. The initial data used in the simulations shown here were produced with the additional assumption of irrotationality of the fluid flow, *i.e.* the condition in which the spins of the stars and the orbital motion are not locked; instead, they are defined so as to have vanishing vorticity. Initial data obtained with the alternative assumption of rigid rotation were not used because, differently from what happens for binaries consisting of ordinary

² Stated differently, we evolve only the region $\{x \geq 0, z \geq 0\}$ applying a 180°-rotational-symmetry boundary condition across the plane at $x = 0$.

TABLE IV: Properties of the initial grids: number of refinement levels (including the coarsest grid); number of finer levels that are moved to follow the stars; spacing of the finest level; length of the side of the finest level; spacing of the coarsest level; outer-boundary location. All lengths are expressed in km. HR, MR, and LR denote the high, medium, and low resolutions, respectively. For `Whisky` the two resolutions are in a ratio of 5/4, while for `SACRA` the ratio between LR and MR is 50/42 and the ratio between MR and HR is 1.16.

Model	n° of levels	n° of moving levels	finest spacing	extent of finest grid	coarsest spacing	outer-boundary location
Whisky ideal fluid	6	2	0.1773	44.33	5.67	380
Whisky piecewise, HR	6	2	0.1773	44.33	5.67	760
Whisky piecewise, LR	6	2	0.2216	44.33	7.09	760
SACRA ideal fluid	8	4	0.1387	6.656	17.75	852
SACRA piecewise, HR	7	4	0.1746	9.428	11.17	603
SACRA piecewise, MR	7	4	0.2025	10.13	12.96	648
SACRA piecewise, LR	7	4	0.2411	10.13	12.96	648

stars, relativistic-star binaries are not thought to achieve synchronization (or corotation) in the timescale of the coalescence [66].

The initial models for the binaries have been chosen so as to allow significant possibilities of comparison between the codes and at the same time to limit the required computational time. In particular, after performing several orbits and merging, prompt collapse to a Kerr black hole occurs. As said above, we chose two EoSs, the ideal-fluid EoS (41)³ and a piecewise-polytropic EoS (43). For the latter, the initial data have been kindly provided by K. Taniguchi. Note that the model with the ideal-fluid EoS has been often used in previous work (e.g. [1, 3]).

Some of the physical quantities of the initial configurations are reported in Table III. In brief, they are equal-mass configurations with an initial proper distance between stellar centers of about 60 km (initial orbital frequency 0.303 kHz and 0.265 kHz, respectively for the ideal-fluid model and for the piecewise-polytropic model). The chosen rest masses of $M_0^{\text{IF}} = 1.779 M_{\odot}$ and $M_0^{\text{PP}} = 1.502 M_{\odot}$, respectively for the two models, lead - as desired - to prompt collapse to black hole.

G. Specific grid setup for the reported simulations

For the higher-resolution run with `Whisky`, the spacing of the finest of the six grid levels is $h = 0.120 M_{\odot} \simeq 0.1773$ km and the spacing in the wave zone (the coarsest grid) is $h = 3.84 M_{\odot} \simeq 5.67$ km. For the lower-resolution run the spacing is $h = 0.150 M_{\odot} \simeq 0.2216$ km on the finest grid and $h = 4.80 M_{\odot} \simeq 7.09$ km on the coarsest grid. The finest grid always covers the whole stars. For the simulations with the ideal-fluid model the outer boundary is located at about 380km while in the case of the piecewise-polytropic model, for both resolutions, the outer boundary is at about 760 km. Except for the outer boundary location and the grid spacing, the AMR grid structure was the same for all the runs.

For the runs with `SACRA`, for the ideal-fluid model, the grid structure is essentially the same as in [3]; the finest of the eight grid levels has $h = 0.0938 M_{\odot} \simeq 0.1387$ km. For the simulations with the piecewise polytrope, the computational domain is composed of seven grid levels with the finest grid resolution being $h = 0.1182 M_{\odot} \simeq 0.1746$ km at the high resolution, $h = 0.1370 M_{\odot} \simeq 0.2025$ km at the medium resolution, and $h = 0.1631 M_{\odot} \simeq 0.2411$ km at the lower resolution. The resolution in the wave zone (for the coarsest grid level) is $h \simeq 11.17$ km for the high-resolution run and $h \simeq 12.96$ km for the others. The boundary of the finest grid is at 60% of the stellar radius (along a coordinate axis, at $t = 0$) while the second finest grid covers all the stars for the run with the ideal-fluid EoS, whereas for the run with the piecewise-polytropic EoS, the finest grid covers the stellar radius completely (the boundary of the finest grid is at 115% of the stellar radius). The outer boundary is at about 852 km for the simulations performed with the ideal-fluid EoS and at about 603 km or 648 km for those performed with the piecewise-polytropic EoS, for the high-resolution run and the other runs respectively.

As already noted in Sec. II E, another difference between the grid setups of the two codes is the adopted symmetry. Both codes compute only the $z \geq 0$ portion of the $\{x, y, z\}$ Cartesian coordinate numerical domain, but, while `SACRA` calculates all the $z \geq 0$ portion, `Whisky` calculates only the $x \geq 0$ part of the remaining domain, taking advantage of the 180° degree rotation symmetry characterising equal-mass binaries.

The properties of the grids adopted in the simulations with the two codes are summarised in Table IV.

For the setup of the piecewise-polytrope high-resolution run, `Whisky`, which heavily exploits large parallel facilities, uses approximately 22×10^6 grid points and the total required memory for the high-resolution run is about 640 GBytes. `SACRA`, instead, which has been specifically developed for being able to perform production simulations even on a laptop computer, uses about 7×10^6 grid points and about 11.6 GBytes of memory. For `Whisky`, the total CPU time for the high-resolution piecewise-polytrope run was about 450 CPU hours on 320 processors of the Ranger cluster (at the Texas Advanced Computing Center; the processors are AMD Opteron Quad-Core 64-bit, with clock frequency 2.3 GHz) and for `SACRA` it was about 2000 CPU hours on a Quad-Core machine of Core-i7X processors with clock frequency 3.33

³ The initial data for the simulations adopting the ideal-fluid EoS are set up as a simple polytropic EoS with polytropic constant $K = 123.6$ (in units of $c = G = M_{\odot} = 1$).

GHz.

III. COMPARISON OF THE RESULTS

As also described in [2, 3], the chosen initial data for the present study are such that the stars orbit about 3 times and 7 times, respectively for the two models with different EoSs, before merging. As can be seen in Fig. 1, the rest-mass density at the stellar centres remains approximately constant for the first 6 ms (in the case of the simulation with the ideal-fluid EoS) or 15 ms (for the piecewise-polytropic case) and then decreases, indicating an expansion of the stars due to the tidal force, just before the merger. As expected from the (high) mass of the chosen models, the merged object then immediately collapses to a black hole and the AH is measured for the first time at about 8 and 18 milliseconds, respectively for the two models with different EoSs (*cf.* the highest resolutions). The mass M_{BH} and the angular-momentum parameter $a \equiv J_{\text{BH}}/(M_{\text{BH}})^2$ of the resulting black hole are measured by both codes. The values after the ringdown for the piecewise-polytropic EoS are $M_{\text{BH}}^{\text{Whisky}} = 2.633M_{\odot}$, $M_{\text{BH}}^{\text{SACRA}} = 2.637M_{\odot}$ (a relative difference of 0.15%), and $a^{\text{Whisky}} = 0.79$, $a^{\text{SACRA}} = 0.80$ (a relative difference of 1.2%). For the ideal-fluid EoS the values of the black hole are $M_{\text{BH}}^{\text{Whisky}} = 3.22M_{\odot}$, $M_{\text{BH}}^{\text{SACRA}} = 3.21M_{\odot}$, and $a = 0.84$ for both codes.

Having briefly summarised the dynamics of the system, we present now first a comparison between some quantities produced in evolutions performed with SACRA and with Whisky, each in what is thought to be a good configura-

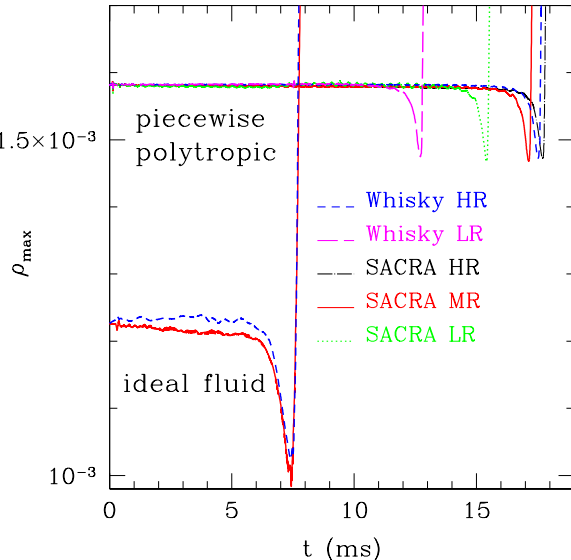


FIG. 1: (Colour online) Comparison of the time evolution of the maximum of the rest-mass density for the two models (with different EoSs) described in Sec. II D 2. For ease of interpretation, we remind the reader that in our units $\rho = 1 \times 10^{-3}$ corresponds approximately to $6.18 \times 10^{14} \text{ g/cm}^3$.

tion in terms of accuracy, violation of the ADM constraints, and cleanliness of gravitational waves. Furthermore, for the piecewise-polytropic EoS we present for each code results obtained at two or three resolutions.

From Fig. 1 one can see immediately that the time of the merger depends considerably on the grid resolution, for both codes, but in a stronger fashion for Whisky. As is well known, the conservation of the angular momentum in numerical simulations of binary compact objects is a delicate issue, which can have very visible effects like the ones in Fig. 1. Even if the merger and post-merger dynamics may not be sensible to the exact timing of the inspiral, the phase of gravitational waves is affected and so this effect must be carefully taken into account when producing templates for gravitational-wave data analysis. For example, [3] attempted to do so by estimating, given a specific initial-data configuration, the 'real' merger time at infinite resolution through an extrapolation based on the results of simulations of the same model at different resolutions. Anyway, we are here interested in the comparison of the codes and note that, when the differences due to the resolution are subtracted by time-shifting the curves, the evolutions of the rest-mass density in the two codes are very similar. As said, a proper analysis of the phase difference of the gravitational waves from the various codes and resolutions will be reported in a future work [18].

We continue the discussion of the results in a more quantitative manner by comparing the time evolution of the rest mass, which should be a conserved quantity as no matter is seen leaving the numerical domain through the outer boundary during the simulation. One can see in the left panel of Fig. 2 that both codes conserve the rest mass at very high accuracy, but in SACRA the violation is of the order of 10^{-3} while in Whisky it is of the order of 10^{-8} . More in detail, the dot-dashed black line refers to the high-resolution SACRA run, which of course shows an improvement over the medium (continuous red line) and lower-resolution ones (dotted green line). The convergence is achieved approximately at second order. The curves referring to Whisky look constant on the main panel, but in the subpanel one can notice the minute increase in the rest mass even in the high-resolution results (short-dashed blue line). The curve referring to the low resolution (long-dashed magenta) drops at the time of AH formation because the matter inside the horizon is not included in the computation of the rest mass.

The reason of the relatively worse conservation in SACRA (as said, the conservation is very good in absolute terms also for SACRA) is to be found in the presence of a refinement boundary very close to the stellar surface. In the orbital phase, oscillations due to the tidal deformation of the NS cause the matter to cross the finest refinement level and the small errors due to the interpolation in the buffer zones are larger where the density is larger. Also in Whisky, if a refinement boundary is placed inside the stars, the violation of the conservation of the rest mass is larger ($\sim 10^{-4}$).

The right panel of Fig. 2, which - as the left one - refers to the piecewise-polytropic EoS, shows then the conservation of the energy, namely the sum of the ADM mass computed on the numerical domain and of the energy carried by gravita-

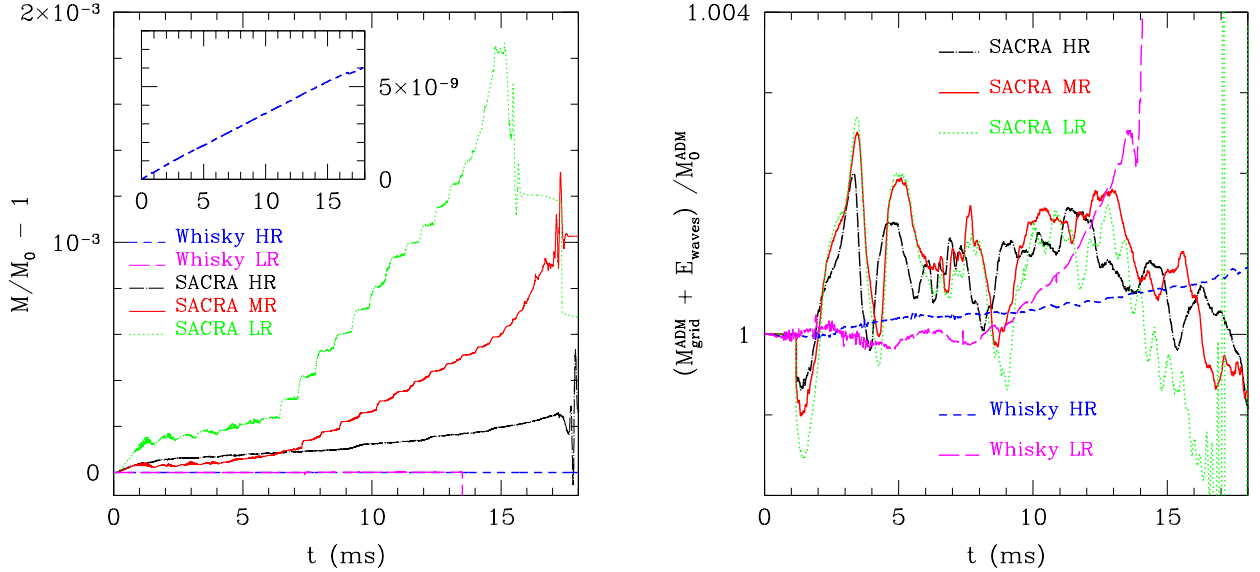


FIG. 2: (Colour online) Left: Comparison of the time evolution of the rest mass (normalised to the initial value). The inset is a magnification of the higher-resolution Whisky curve, in the form $M/M_0 - 1$. These data refer to the piecewise-polytropic EoS. As explained in the text, the larger variations in the SACRA data are due to the choice of grid structure. Right: Comparison of the time evolution of the sum (normalised to the initial value) of the ADM mass measured on the numerical grid and the energy carried away from the grid by gravitational waves. This quantity should be conserved. These data refer to the piecewise-polytropic EoS. Note that the data for the low resolution of Whisky are not reliable after the formation of the AH ($t \simeq 13.4$ ms for this simulation), because the volume integral with which the ADM mass is computed contained also the points inside the horizon. See text for more details.

tional waves outside the numerical domain. Such a quantity, normalised to its initial value (the initial ADM mass) should be constant and the figure shows the deviation of the results from constancy. The colours and line types are the same as in the left panel. At the highest resolutions, both Whisky and SACRA conserve this quantity very well, at the order of 1 per 1000 during the inspiral and at better than 1% overall.

Some of the differences in the curves referring to the two codes (in particular the 'smoothness') are due to the different way of computing the ADM mass. Whisky performs a volume integral with the formula

$$M_{ADM, Vol} = \int_V \partial_i [\alpha \sqrt{\gamma} \gamma^{jk} \gamma^{li} (\partial_k \gamma_{jl} - \partial_l \gamma_{jk})] d^3x \quad (49)$$

and in the simulations of this work it does not exclude the points inside the AH from the computation, so the values of the ADM mass given by Whisky after the appearance of the AH are affected by gross errors. SACRA, instead, uses a surface integral on a spherical surface far from the central objects. This method gives consistent results after the formation of the AH, but is more sensitive to small metric oscillations in the vicinity of the chosen surfaces, which lie in the coarse resolution region; the 'roughness' of the curves follows from this.

Figure 3, which refers to the piecewise-polytropic EoS, shows then the conservation of the angular momentum, defined here as the sum of the angular momentum computed on the numerical domain and of the angular momentum carried by gravitational waves outside the numerical domain. Such a quantity, normalized to its initial value (the initial angular

momentum) should be constant and the figure shows the deviation of the results from constancy. The colours and line types are the same as in the previous figures. At the highest resolution, Whisky conserves this quantity very well, at better than 1%, and also for SACRA deviations from constancy are of the same order, even if larger oscillations are visible. The difference in the computation of the angular momentum, analogous to the one for the ADM mass, is also here at the origin of the difference in the smoothness of the curves. Namely, Whisky performs a volume integral with the formula [69]

$$J_{vol}^i = \varepsilon^{ijk} \int_V \left(\frac{1}{8\pi} \tilde{A}_{jk} + x_j S_k + \frac{1}{12\pi} x_j K_{,k} + \right. \\ \left. - \frac{1}{16\pi} x_j \tilde{\gamma}^{lm} ,_k \tilde{A}_{lm} \right) e^{6\phi} d^3x \quad (50)$$

and excludes from the integral the points inside the AH. However, if the angular momentum of the black hole is added to the one computed above, the correct time evolution of the quantity in Fig. 3 is recovered, except for an interval just after the AH formation, when the AH is small and covers only a few grid points, and so the measurement of its angular momentum is inaccurate. SACRA, instead, uses also here a surface integral.

As previously noted, also from the time evolutions in Fig. 3 one sees that the conservation of the angular momentum at these resolutions depends in a stronger way on resolution for the Whisky code with respect to SACRA. In addition, one can see that, while also the SACRA data show convergence almost everywhere, in some time intervals the behaviour at different resolutions is not convergent, for example at the spike around 2.5 ms. The reason is not completely clear at

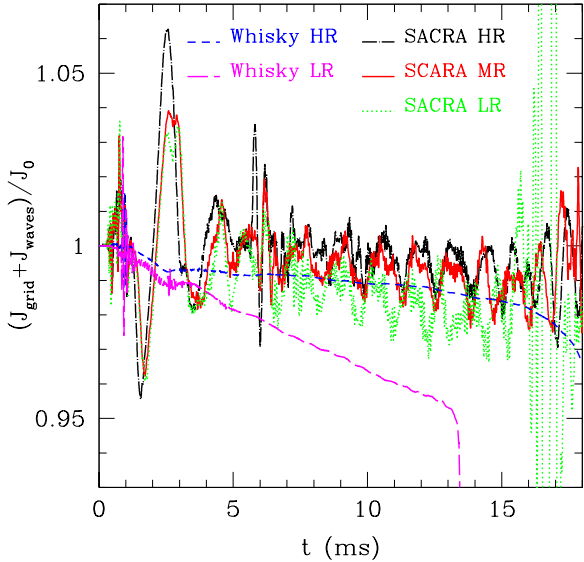


FIG. 3: (Colour online) Comparison of the time evolution of the angular momentum, computed as the sum of the angular momentum measured on the numerical grid and the angular momentum carried away from the grid by gravitational waves. These data refer to the piecewise-polytropic EoS. As already noted for Fig. 2, also here the data for the low resolution of Whisky are not reliable after the formation of the AH ($t \simeq 13.4$ ms for this simulation), because the volume integral with which the angular momentum is computed excludes the contribution of the black hole. See text for more details.

the moment, but we think that this is probably related to the low resolution of the coarsest grid, where the surface on which the angular momentum is computed is located [note that accurate extraction of angular momentum requires an accurate computation of parts of the extrinsic curvature that are $O(r^{-3})$ and these are much smaller than the leading-order wave part of $O(r^{-1})$]. If the angular momentum is computed on surfaces that lie on the finer levels, the differences in the wrong direction caused by resolution are much smaller (but the value of the angular momentum is less accurate).

We now proceed to analyze gravitational waves extracted from the simulations. The data presented here are extracted from the numerical simulations at distances from the origin of the axes in the interval $300 \sim 600$ km. For building templates to be used in the analysis of the data taken by the gravitational-wave detectors, the accurate knowledge of the frequency of the waves is of special importance. Thus we first show in the left panel of Fig. 4, which refers to the ideal-fluid EoS, the comparison of the orbital frequency. The agreement of the results of the two codes is excellent, if one ignores the initial spurious signal (related to the spurious gravitational-wave content of the initial data, which is rapidly propagated away). The orbital frequency Ω is computed in postprocessing

from the time derivatives of the real and imaginary part of ψ_4 :

$$\Omega = -\frac{d}{dt} \left[\text{atan} \frac{\Im(\psi_4)}{\Re(\psi_4)} \right] = -\frac{\frac{d\Im(\psi_4)}{dt} \Re(\psi_4) - \Im(\psi_4) \frac{d\Re(\psi_4)}{dt}}{[\Re(\psi_4)]^2 + [\Im(\psi_4)]^2}. \quad (51)$$

The biggest real (*i.e.* not related to the noise) difference between the two curves is during the merger, at around 7.5 ms and it is of about 10%, which is consistent with the results of [7].

In the right panel of Fig. 4 we plot the amplitude of waves as a function of the frequency. The inset shows that the error on the amplitude is always at most 10%, which is of the same order of magnitude of the one found in the comparison of numerical codes in binary-black-hole simulations [7] and provides here an important consistency check on the numerical accuracy and validity of the waveforms of both Whisky and SACRA. The discussion of whether, as in [7], also for binary-NS-merger waveforms this discrepancy is relevant or not for data analysis (namely whether current detectors can or cannot distinguish between the waveforms of the two codes) is left to a future work, now in preparation [18].

Finally, in order to give also a strong visual support to the goodness of the consistence of gravitational waves computed from the two codes, in Fig. 5, which refers to the piecewise-polytropic EoS, we show the $(h_+)_22$ waveforms, together with the curve predicted by the Taylor-T4 post-Newtonian approximation [18, 67, 68]. These are the raw data, in the sense that no phase shift is performed to achieve the best alignment of gravitational waves. The latter procedure is often successfully performed in data-analysis related work and will be included in our future work [18]. Nevertheless the similarity of the numerical waveforms (both between themselves and with respect to the post-Newtonian prediction) in the inspiral part is astonishingly good at the highest resolutions adopted here (see upper panel of Fig. 5). On the contrary, the lower resolutions (lower panel) are clearly not good enough.

The situation is somewhat different after the merger. The ringdown part shows agreement between the two codes, but the waves show some differences both in amplitude and frequency in the interval after the merger and before the ringdown. This is due to the differences in the EoSs, as explained in Sec. II D 2. Namely, in the present simulations SACRA added a thermal part to the piecewise-polytropic EoS, while Whisky did not. As shown by the figures, the difference in the EoS are irrelevant to the inspiral phase, but not so after the merger, as expected.

IV. CONCLUSIONS

In this work we have presented the first, detailed comparison of two general-relativistic hydrodynamics codes, the Whisky code and the SACRA code.

We have compared numerical-relativity waveforms and other quantities for the last orbits, merger, and collapse of equal-mass irrotational binary NS systems, as produced by the two independent computer codes. We focused on two analytic EoSs, namely the simple ideal-fluid EoS and a piecewise-

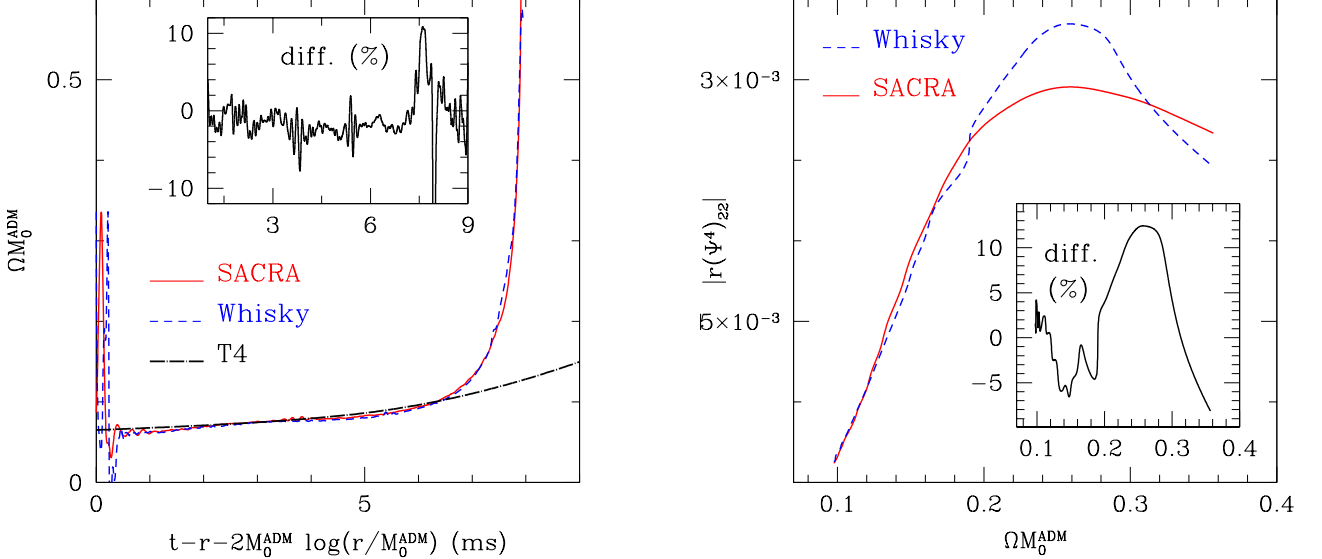


FIG. 4: (Colour online) Left: Comparison of the time evolution of the orbital frequency, computed from ψ_4 . These data refer to the ideal-fluid EoS. The inset shows the percent difference of the two curves. The curve labeled T4 is the Taylor-T4 post-Newtonian approximation [18, 67, 68]. Right: Comparison of the amplitude of the wave as a function of the frequency $M\Omega$. The inset shows the percent difference between the two curves. These data refer to the ideal-fluid EoS.

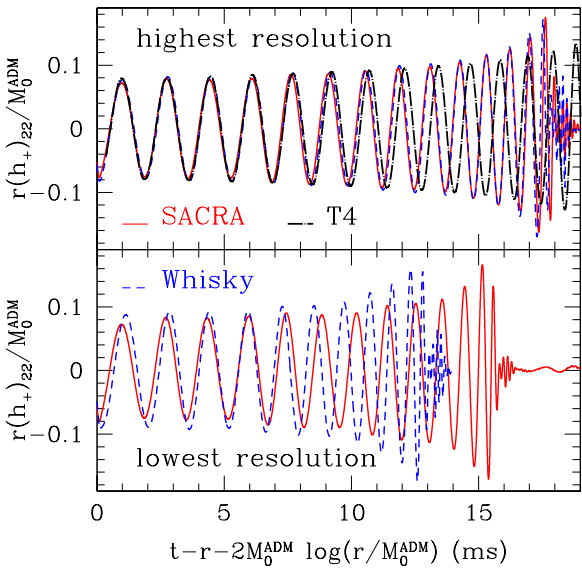


FIG. 5: (Colour online) Comparison of the waveform $(h_+)_22$. These data refer to the piecewise-polytropic EoS. The upper panel refers to the “highest resolution” and the lower panel to the “lowest resolution” (see text for details). As in Fig. 4, the curve labeled T4 is the Taylor-T4 post-Newtonian approximation [18, 67, 68].

polytropic EoS, for which we additionally presented more resolutions. The purpose was to perform a stringent consistency check of the results from these codes. We found that the waveform frequency and amplitude computed with the two codes are in agreement with a discrepancy of at most 10% (this es-

timate refers to the merger time; the discrepancy is much less during the inspiral), which is comparable to the intrinsic error of each individual code at the adopted resolutions. We stress the fact that this estimated error should be considered here an upper limit and that the discrepancy between the waves computed in the two codes will be smaller when we will consider an optimised overlap of the waveforms, in our future work [18].

The comparison of purely hydrodynamical quantities, like the rest-mass density, shows better results, with a difference between the two codes of at most about 1%. This number refers however only to global quantities (like maxima and norms), but not to point-to-point comparisons, mainly because of the small phase difference in the evolution, which makes pointwise comparisons meaningless. In fact, even after compensating for the phase difference, errors larger than 1% are seen at some points, noticeably those near the surface of the stars. Such errors are related to different implementations of, e.g., the atmosphere treatment and do not influence the global dynamics in a noticeable way.

Finally, by comparing other time-dependent spacetime and matter quantities, we showed that both codes conserve at high accuracy rest mass, energy, and angular momentum, when taking into account the emission of gravitational waves. The small differences that are present have been related to details in the different implementations and grid setups.

In conclusion, encouraging results have been shown and more work is now necessary to assess how the remaining differences in the results may affect the construction of templates for gravitational-wave data analysis. This will be the subject of a future work [18], which may include also more codes in the comparison.

Acknowledgments

We are grateful to K. Taniguchi for providing the initial data we used in this work and to the Meudon group for producing and making public a code very useful to the community. LB thanks B. Giacomazzo, I. Hawke, J. Read, L. Rezzolla, and E. Schnetter for useful comments and discussion, and acknowledges the continuous and great work done by the community developing the *Cactus* and the *Carpet* codes. The *Whisky* simulations were performed on the Ranger clus-

ter at the Texas Advanced Computing Center through TERA-GRID allocation TG-MCA02N014 and at the CFCA of the National Astronomical Observatory of Japan. The work of LB was supported in part by the JSPS Postdoctoral Fellowship For Foreign Researchers, Grant-in-Aid for Scientific Research (19-07803), and by the Grant-in-Aid for Young Scientists (22740163); the work of MS was supported by the Grant-in-Aid for Scientific Research (21340051), and by the Grant-in-Aid for Scientific Research on Innovative Area (20105004) of the Japanese MEXT.

-
- [1] L. Baiotti, B. Giacomazzo, and L. Rezzolla, *Class. Quantum Grav.* **26**, 114005 (2009).
- [2] L. Baiotti, B. Giacomazzo, and L. Rezzolla, *Phys. Rev. D* **78**, 084033 (2008).
- [3] T. Yamamoto, M. Shibata, and K. Taniguchi, *Phys. Rev. D* **78**, 064054 (2008).
- [4] F. Pretorius, *Phys. Rev. Lett.* **95**, 121101 (2005).
- [5] M. Campanelli, C. O. Lousto, P. Marronetti, and Y. Zlochower, *Phys. Rev. Lett.* **96**, 111101 (2006).
- [6] J. G. Baker, J. Centrella, D.-I. Choi, M. Koppitz, and J. van Meter, *Phys. Rev. Lett.* **96**, 111102 (2006).
- [7] M. Hannam et al., *Phys. Rev. D* **79**, 084025 (2009).
- [8] J. G. Baker, M. Campanelli, F. Pretorius, and Y. Zlochower, *Class. Quantum Grav.* **24**, S25 (2007).
- [9] B. Brügmann, J. A. González, M. Hannam, S. Husa, U. Sperhake, and W. Tichy, *Phys. Rev. D* **77**, 024027 (2008), gr-qc/0610128.
- [10] LIGO, IIGO – <http://www.ligo.caltech.edu/>.
- [11] VIRGO, vIRGO – <http://www.virgo.infn.it/>.
- [12] GEO, gEO600 – <http://www.geo600.uni-hannover.de/>.
- [13] M. Punturo et al., *Class. Quantum Grav.* **27**, 084007 (2010).
- [14] Einstein Telescope, URL <http://www.et-gw.eu>.
- [15] L. Baiotti, I. Hawke, P. Montero, and L. Rezzolla, in *Computational Astrophysics in Italy: Methods and Tools*, edited by R. Capuzzo-Dolcetta (MSAIt, Trieste, 2003), vol. 1, p. 210.
- [16] L. Baiotti, I. Hawke, P. J. Montero, F. Löffler, L. Rezzolla, N. Stergioulas, J. A. Font, and E. Seidel, *Phys. Rev. D* **71**, 024035 (2005).
- [17] B. Giacomazzo and L. Rezzolla, *Class. Quantum Grav.* **24**, S235 (2007).
- [18] L. Baiotti, J. D. E. Creighton, J. L. Friedman, B. Giacomazzo, C. Markakis, J. S. Read, L. Rezzolla, M. Shibata, K. Taniguchi, et al., in preparation (2010).
- [19] E. Nakar, *Phys. Rep.* **442**, 166 (2007).
- [20] D. Pollney, C. Reisswig, L. Rezzolla, B. Szilágyi, M. Ansorg, B. Deris, P. Diener, E. N. Dorband, M. Koppitz, A. Nagar, et al., *Phys. Rev. D* **76**, 124002 (2007).
- [21] T. Nakamura, K. Oohara, and Y. Kojima, *Prog. Theor. Phys. Suppl.* **90**, 1 (1987).
- [22] M. Shibata and T. Nakamura, *Phys. Rev. D* **52**, 5428 (1995).
- [23] T. W. Baumgarte and S. L. Shapiro, *Phys. Rev. D* **59**, 024007 (1998).
- [24] M. Alcubierre, B. Brügmann, T. Drumlitsch, J. A. Font, P. Papadopoulos, E. Seidel, N. Stergioulas, and R. Takahashi, *Phys. Rev. D* **62**, 044034 (2000).
- [25] T. Goodale, G. Allen, G. Lanfermann, J. Massó, T. Radke, E. Seidel, and J. Shalf, in *Vector and Parallel Processing – VECPAR’2002, 5th International Conference, Lecture Notes in Computer Science* (Springer, Berlin, 2003).
- [26] J. W. York, in *Sources of gravitational radiation*, edited by L. L. Smarr (Cambridge University Press, Cambridge, UK, 1979), pp. 83–126, ISBN 0-521-22778-X.
- [27] M. Alcubierre, B. Brügmann, P. Diener, M. Koppitz, D. Pollney, E. Seidel, and R. Takahashi, *Phys. Rev. D* **67**, 084023 (2003).
- [28] C. W. Misner, K. S. Thorne, and J. A. Wheeler, *Gravitation* (W. H. Freeman, San Francisco, 1973).
- [29] C. Bona, J. Massó, E. Seidel, and J. Stela, *Phys. Rev. Lett.* **75**, 600 (1995).
- [30] J. G. Baker, J. Centrella, D.-I. Choi, M. Koppitz, and J. van Meter, *Phys. Rev. Lett.* **96**, 111102 (2006).
- [31] J. van Meter, J. G. Baker, M. Koppitz, and D.-I. Choi, *Phys. Rev. D* **73**, 124011 (2006).
- [32] M. Koppitz, D. Pollney, C. Reisswig, L. Rezzolla, J. Thornburg, P. Diener, and E. Schnetter, *Phys. Rev. Lett.* **99**, 041102 (2007).
- [33] J. Thornburg, *Class. Quantum Grav.* **21**, 743 (2004).
- [34] J. Thornburg, *Phys. Rev. D* **54**, 4899 (1996).
- [35] A. Ashtekar, C. Beetle, and S. Fairhurst, *Class. Quantum Grav.* **17**, 253 (2000).
- [36] A. Ashtekar, C. Beetle, O. Dreyer, S. Fairhurst, B. Krishnan, J. Lewandowski, and J. Wisniewski, *Phys. Rev. Lett.* **85**, 3564 (2000).
- [37] A. Ashtekar, C. Beetle, and J. Lewandowski, *Phys. Rev. D* **64**, 044016 (2001).
- [38] A. Ashtekar and B. Krishnan, *Phys. Rev. Lett.* **89**, 261101 (2002).
- [39] O. Dreyer, B. Krishnan, D. Shoemaker, and E. Schnetter, *Phys. Rev. D* **67**, 024018 (2003).
- [40] L. Gunnarsen, H. Shinkai, and K. Maeda, *Class. Quantum Grav.* **12**, 133 (1995).
- [41] S. A. Teukolsky, *Astrophys. J.* **185**, 635 (1973).
- [42] L. Baiotti, S. Bernuzzi, G. Corvino, R. De Pietri, and A. Nagar, *Phys. Rev. D* **79**, 024002 (2009).
- [43] V. Moncrief, *Annals of Physics* **88**, 323 (1974).
- [44] J. M. Martí, J. M. Ibáñez, and J. A. Miralles, *Phys. Rev. D* **43**, 3794 (1991).
- [45] F. Banyuls, J. A. Font, J. M. Ibáñez, J. M. Martí, and J. A. Miralles, *Astrophys. J.* **476**, 221 (1997).
- [46] J. Ibáñez, M. Aloy, J. Font, J. Martí, J. Miralles, and J. Pons, in *Godunov methods: theory and applications*, edited by E. Toro (Kluwer Academic/Plenum Publishers, New York, 2001).
- [47] J. A. Font, *Living Rev. Relativ.* **6**, 4 (2003).
- [48] E. F. Toro, *Riemann Solvers and Numerical Methods for Fluid Dynamics* (Springer-Verlag, 1999).
- [49] S. A. Teukolsky, *Phys. Rev. D* **61**, 087501 (2000).
- [50] G. Leiler and L. Rezzolla, *Phys. Rev. D* **73**, 044001 (2006).
- [51] P. Colella and P. R. Woodward, *J. Comput. Phys.* **54**, 174

- (1984).
- [52] A. Kurganov and E. Tadmor, *J. Comput. Phys.* **160**, 241 (2000).
 - [53] A. Harten, P. D. Lax, and B. van Leer, *SIAM Rev.* **25**, 35 (1983).
 - [54] M. A. Aloy, J. M. Ibáñez, J. M. Martí, and E. Müller, *Astrophys. J. Supp.* **122**, 151 (1999).
 - [55] B. Giacomazzo, L. Rezzolla, and L. Baiotti, *MNRAS* **399**, L164 (2009).
 - [56] J. S. Read, B. D. Lackey, B. J. Owen, and J. L. Friedman, *Phys. Rev. D* **79**, 124032 (2009).
 - [57] J. S. Read, C. Markakis, M. Shibata, K. Uryu, J. D. E. Creighton, and J. L. Friedman, *Phys. Rev. D* **79**, 124033 (2009).
 - [58] M. J. Berger and J. Oliger, *J. Comput. Phys.* **53**, 484 (1984).
 - [59] E. Schnetter, S. H. Hawley, and I. Hawke, *Class. Quantum Grav.* **21**, 1465 (2004).
 - [60] A. Harten, B. Engquist, S. Osher, and S. R. Chakrabarty, *J. Comput. Phys.* **71**, 231 (1987).
 - [61] B. Bruegmann, J. A. Gonzalez, M. Hannam, S. Husa, and U. Sperhake, *Phys. Rev. D* **77**, 124047 (2008).
 - [62] H. O. Kreiss and J. Oliger, *Methods for the approximate solution of time dependent problems* (GARP publication series No. 10, Geneva, 1973).
 - [63] E. Gourgoulhon, P. Grandclément, K. Taniguchi, J. A. Marck, and S. Bonazzola, *Phys. Rev. D* **63**, 064029 (2001).
 - [64] K. Taniguchi and E. Gourgoulhon, *Phys. Rev. D* **66**, 104019 (2002).
 - [65] URL <http://www.lorene.obspm.fr>.
 - [66] L. Bildsten and C. Cutler, *Astrophys. J.* **400**, 175 (1992).
 - [67] J. G. Baker, J. R. van Meter, S. T. McWilliams, J. Centrella, and B. J. Kelly, *Phys. Rev. Letters* **99**, 181101 (2007).
 - [68] M. Boyle, D. A. Barrow, L. E. Kidder, A. H. Mroué, H. P. Pfeiffer, M. A. Scheel, G. B. Cook, and S. A. Teukolsky, *Phys. Rev. D* **76**, 124038 (2007).
 - [69] M. Shibata, *Phys. Rev. D* **60**, 104052 (1999).